RMetS
Royal Meteorological Society

A potential vorticity signature for the cold sector of winter extratropical cyclones

Benoît Vannière,[a]* Arnaud Czaja,[a] Helen Dacre,[b] Tim Woollings[c] and Rhys Parfitt[a]

[a]*Physics Department, Imperial College London, UK*
[b]*Department of Meteorology, University of Reading, UK*
[c]*Atmospheric Physics Clarendon Laboratory, Oxford University, UK*

*Correspondence to: B. Vannière, Space and Atmospheric Physics Group, Department of Physics, Imperial College, Huxley Building, Room 716, London, SW7 2AZ, UK. E-mail: b.vanniere@imperial.ac.uk

The cold sector of a midlatitude storm is characterized by distinctive features such as strong surface heat fluxes, shallow convection, convective precipitation and synoptic subsidence. In order to evaluate the contribution of processes occurring in the cold sector to the mean climate, an appropriate indicator is needed. This study describes the systematic presence of negative potential vorticity (PV) behind the cold front of extratropical storms in winter. The origin of this negative PV is analyzed using ERA-Interim data, and PV tendencies averaged over the depth of the boundary layer are evaluated. It is found that negative PV is generated by diabatic processes in the cold sector and by Ekman pumping at the low centre, whereas positive PV is generated by Ekman advection of potential temperature in the warm sector. We suggest here that negative PV at low levels can be used to identify the cold sector. A PV-based indicator is applied to estimate the respective contributions of the cold sector and the remainder of the storm to upward motion and large-scale and convective precipitation. We compare the PV-based indicator with other distinctive features that could be used as markers of the cold sector and find that potential vorticity is the best criterion when taken alone and the best when combined with any other.

Key Words: cold sector; potential vorticity; extratropical cyclone; boundary layer

Received 15 December 2014; Revised 19 August 2015; Accepted 2 September 2015; Published online in Wiley Online Library 9 October 2015

1. Introduction

Cold-air outbreaks are a common feature of the Western North Atlantic basin in boreal winter, when rapidly intensifying extratropical cyclones bring cold and dry polar air off North America (Grossman and Betts, 1990; Kolstad and Bracegirdle, 2008). The thermal contrast of the cold air mass with the warmer waters is responsible for the largest wintertime heat transfers (sensible and latent) from ocean to atmosphere on Earth (Wayland and Raman, 1989; Zolina and Gulev, 2003). As it is advected by synoptic winds, the air takes up moisture and heat over the ocean and a sequence of processes occurs: a deck of stratus cloud first forms at the top of the boundary layer, stabilized by the subsidence typically occurring behind the cold front, then turns into convective rolls and eventually evolves towards shallow convection (Grossman and Betts, 1990; Chou and Ferguson, 1991). Following the AMS glossary, we define the *cold sector* as the area within a circulation of an extratropical cyclone where relatively cold air can be found and where the processes described above occur. It typically lies behind the cold front.

The Western North Atlantic basin is also a region of marked climatic features. On the atmospheric side, it corresponds to the entrance of the Atlantic storm track (e.g. Hoskins and Valdes, 1990; Brayshaw *et al.*, 2011), which is closely related to deep latent heating (e.g. Hoskins and Valdes, 1990). On the oceanic side, the Gulf Stream current, which flows along the North American continental margin, carries warmer waters northward, leading to strong sea-surface temperature (SST) gradients off the coast and further east. The SST front has a substantial impact on the marine atmospheric boundary layer above: *QuikSCAT* satellite data revealed increased wind speed over warmer waters and coherent structures of surface wind convergence along the SST gradient (Chelton *et al.*, 2004), while *CALIPSO* satellite data captured a sharp low-level cloud transition across the front (Small *et al.*, 2008; Liu *et al.*, 2014). Minobe *et al.* (2008) showed that the wind convergence in the boundary layer anchored a band of precipitation and was accompanied by vertical wind reaching the tropopause. Minobe *et al.* (2010) investigated the seasonality of this signal further: deep structure tended to be observed in summer and remained confined to the boundary layer in winter.

The intense air–sea interaction in the cold sector suggests that synoptic activity may play a significant role in shaping the mean climatic features of the Western North Atlantic basin. Some evidence of this was given by Nelson and He (2012), who demonstrated that the tight relationship between the surface wind convergence, the Laplacian of sea-level pressure (SLP) and the Laplacian of SST, previously stressed by Minobe *et al.* (2008), was well reproduced during 15 days of cold-air outbreaks in a high-resolution coupled model. Young and Sikora (2003) described open cloud bands originating from the meandering of the Gulf Stream during cold-air outbreaks, which play a major role in determining the cloud pattern of much of this oceanic region. Liu *et al.* (2014), in an attempt to explain the enhancement of cloud cover and the increase of cloud-top level over the Gulf Stream front, compared southerly and northerly regimes: under cold northerly advection, strong near-surface instability led to a well-mixed boundary layer over the Gulf Stream, causing a southward deepening of low-level clouds across the SST front.

More fundamentally, several pathways by which SSTs could maintain high baroclinicity in storm tracks have been proposed and they involve different synoptic environments. For instance, the oceanic baroclinic adjustment proposed by Nakamura *et al.* (2008), which assumes that differential heating across the SST frontal gradient restores low-level baroclinicity, is more likely to occur in the cold sector, where surface heat fluxes are larger. In contrast, Hoskins and Valdes (1990) suggested that mid-troposphere diabatic heating along the warm conveyor belt (WCB) was key to explaining the existence of the storm track. Unlike Nakamura *et al.* (2008), this would highlight the warm sector as the region where maintenance of high baroclinicity is achieved.

The example just described suggests that it would be useful, in order to isolate the climatological impact of processes occurring in different synoptic environments, to find a way to partition cold and warm sectors. Several algorithms have been proposed to identify the warm and cold fronts (e.g. Hewson, 1998; Simmonds *et al.*, 2012) and indicators for the WCB have also been developed (e.g. Eckhardt *et al.*, 2004; Madonna *et al.*, 2014). To our knowledge, however, such an indicator has not been used to identify the cold sectors of extratropical storms systematically. (It is worth mentioning, however, the work of Kolstad and Bracegirdle (2008), who used a simple temporal index based on the vertical potential temperature gradient between the sea surface and 700 mb, together with an empirical threshold, to identify cold-air outbreaks in the Atlantic. Their study did not test its possible use as a spatial indicator for the cold sector and it is not obvious whether a constant threshold must be used to select the cold sector in a systematic way.)

A few studies have reported the presence of negative potential vorticity (PV) in the cold sectors of extratropical storms (Stoelinga, 1996; Chagnon *et al.*, 2013). Chagnon *et al.* (2013) showed that negative PV arose from the boundary-layer tendency and was generated by strong positive heat flux (maximum at the surface). However, all these studies were limited to one or a few single events rather than a climatology and the systematic presence of negative PV in the cold sector has, to our knowledge, never been explored. Negative PV in the cold sector of baroclinic storms may have received little attention, because it is not included in classical models of cyclogenesis (e.g. the Eady model has PV equal to 0 uniformly) and because anomalous PV is more often diagnosed than PV itself.

The goal of this article is threefold: (i) show that there is negative PV at the surface in the cold sector of extratropical storms, (ii) find the origin of this negative PV and (iii) demonstrate that negative PV is a useful indicator of the cold sector for climatological studies. The article is structured as follows: data and methods are presented in section 2, the structure of PV in a composite of extratropical cyclones is described in section 3 and Lagrangian PV tendencies in the boundary layer for the composites of storms are calculated and interpreted in section 4 (after reviewing the state of knowledge of PV in the boundary layer in that same section). Finally, the possible use of the negative PV signature of the cold sector as an indicator of this region is discussed in section 5. Section 6 summarizes and discusses the main results.

2. Data and method

2.1. Data

The ERA-Interim dataset is a reanalysis of the global atmosphere covering the period since 1979 and updated continuously in real time (Berrisford *et al.*, 2009; the period retained for the analysis is 1979–2012). It uses 60 vertical levels and a spectral $T255$ truncation (the reduced Gaussian grid has a 79 km spacing for surface and other grid-point fields).

A moist boundary-layer scheme based on eddy diffusion combined with mass flux transport (Köhler, 2005; Köhler *et al.*, 2011) is used in ERA-Interim. The mixed-layer height is determined using an entraining parcel, selecting the top of stratocumulus or cloud base in shallow convection situations. The values at the boundary-layer top of the various fields needed in the calculation of the PV tendencies are determined using a vertical linear interpolation of the fields to the boundary-layer top.

Large-scale and convective precipitation are based on forecast data and accumulated over 3 h. Hawcroft *et al.* (2012) showed that the magnitude of the precipitation rate was not reliable for the first 3–9 h of the forecast, due to spin-up effects, whereas the pattern was not significantly altered. In this study, we are more interested in testing a qualitative partitioning of the precipitation than estimating the true amount of rainfall. Moreover, it is important that PV and precipitation are evaluated over periods as close as possible, so that the PV-based indicator is consistent with the precipitation to which it is applied. These considerations led us to choose the first available 3 h accumulated precipitation in spite of this bias.

2.2. Composites

The study area is the Western North Atlantic basin (65°W–45°W, 34°N–42°N), which corresponds to the entrance of the storm track. Restricting the analysis to a limited spatial domain helps select storms with a similar degree of maturity. This will prove particularly helpful to average the composite in the reference frame of the storm. Indeed, as storms travel further east, their cold fronts rotate around the lowest pressure. Thus, features showing a strong asymmetry on each side of the front are smoothed out in a composite including different stages of storm development (Catto *et al.*, 2010; Dacre *et al.*, 2012).

The technique to detect storms and build the composite is as follows. The cyclone is defined as a point object, identified by a local minimum in sea-level pressure falling in the domain of study. Following Wernli and Schwierz (2006), we define a local minimum of SLP as the case where the SLP of a given point is smaller than its eight immediate neighbours. Thus a single cyclone throughout its evolution could be identified as separate systems on consecutive days. This approach is straightforward, but cannot provide information about the genesis and lysis of cyclones. To maximize the signal-to-noise ratio further, only storms with minimum SLP below the threshold value of 985 mb are considered. The composite thus formed has 57 extratropical cyclones, which correspond approximately to the top 5% of strongest storms in this region.

The composite maps are then formed by centring ERA-Interim grid on the lowest surface pressure for each cyclone.

3. Low-level PV composites

PV is defined from the relation (Hoskins *et al.*, 1985)

$$PV = \frac{1}{\rho}(\zeta_a.\nabla\theta), \tag{1}$$

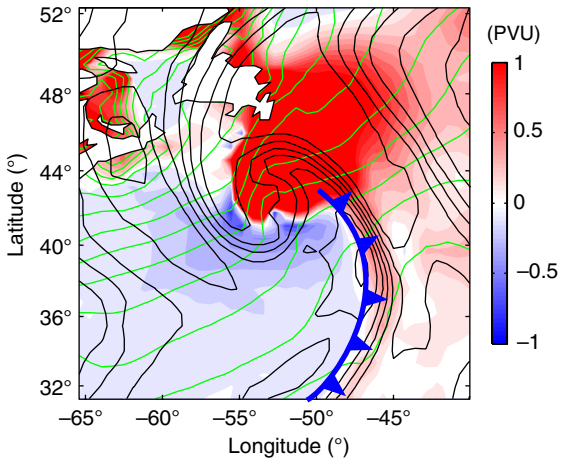

Figure 1. Potential vorticity at 975 mb (in PVU and represented in shadings), potential temperature at surface level (green contours every 5 K) and column relative humidity averaged from the surface to 200 mb (black contours every 10%) on 20 January 2000 at 1200 UTC.

where ρ is the density of air, ζ_a the absolute vorticity vector and θ the potential temperature. Figure 1 displays a snapshot of PV at 975 mb off the coast of North America on 20 January 2000. One observes positive PV to the northeast of the storm centre (roughly coincident with the figure's centre), in the region of the warm front. The vertically integrated relative humidity over the troposphere (black contours) is overlaid to help identify the position of the WCB. The latter has a characteristic 'tau' shape, the main south branch being along the east side of the cold front. A sharp transition in the sign of PV occurs through the cold front, with negative PV behind the cold front and positive PV in the WCB region.

Figure 2(a) shows the composite of PV at 975 mb centred on the lowest pressure of the composite storms (surface isobars are in black contours). The smooth transition from positive to negative PV across the cold front is the result of compositing. During the development of a baroclinic storm, as described by the Norwegian cyclone model, the cold front tends to rotate around the low-pressure minima. In the composite, no correction was applied to rotate back and overlay the cold fronts, resulting in a smoothing of the limit between the cold and warm sectors, which would otherwise be sharper for individual events. PV has been calculated at sea-surface level, by interpolation of values given on pressure levels. In cases where SLP is higher than the lowest pressure level (1000 mb), it is estimated by extrapolating the vertical PV gradient of the lowest pressure level. The results are presented in Figure 2(b) and show that the absolute value of PV is higher at the surface and that areas with positive/negative PV remain unchanged compared with PV taken at 975 mb.

To further assess how frequently a PV airmass of a given sign is found, we display in Figure 3 the frequency of positive PV in the frame of reference of the travelling storm. One observes a clear region of very low frequencies in the southwest quadrant of this plot, demonstrating that the presence of negative PV is a robust feature of the cold sector of storms.

In Figure 4, we decompose the total PV in Eq. (1) into vertical (PV_Z, i.e. $(1/\rho)(\zeta_Z + f).(\partial\theta/\partial z)$) and horizontal ($PV_H$, i.e. $(1/\rho)\zeta_H.\nabla_H\theta$) components. The fact that these fields were recomputed on pressure levels from ERA-Interim data, which provides fewer vertical levels than the original sigma levels, explains the slight discrepancies when comparing the vertical and horizontal components (Figures 4(a) and (b)) to total PV (Figure 2(a)), and in particular the fact that negative PV_Z is slightly overestimated. It is, however, clear from this decomposition that PV_Z provides the main contribution to negative PV in the cold sector: air–sea heat fluxes occurring there are so large that convection is not fast enough to stabilize the temperature profile. This result is consistent with the diagnostic used in Kolstad and

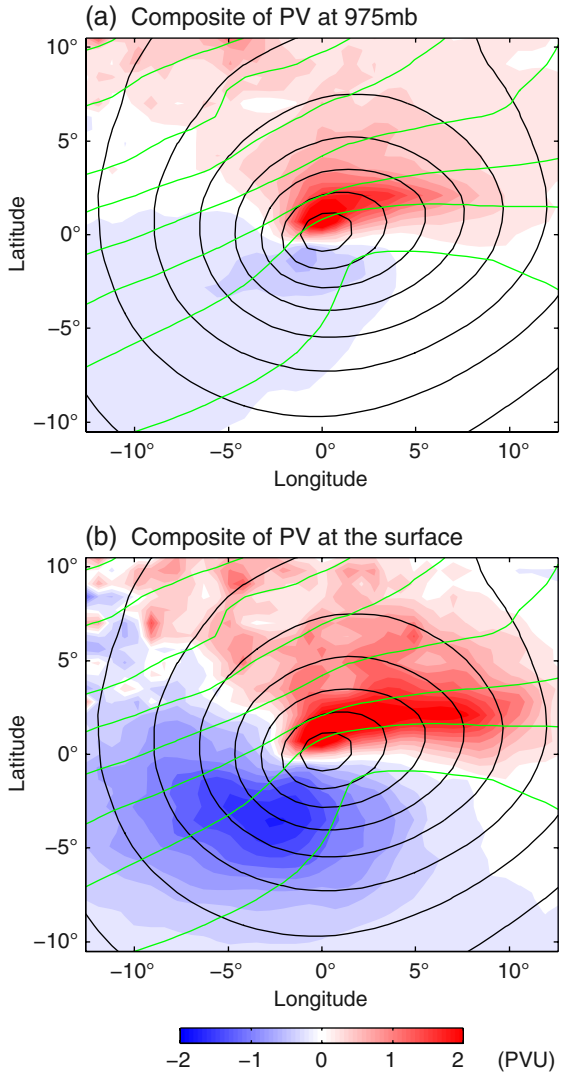

Figure 2. PV (in PVU and represented in shadings) for the composite of extratropical storms: (a) at 975 mb and (b) at surface level. Potential temperature at surface level (green contours every 5 K) and sea-level pressure (black contours every 5 mb).

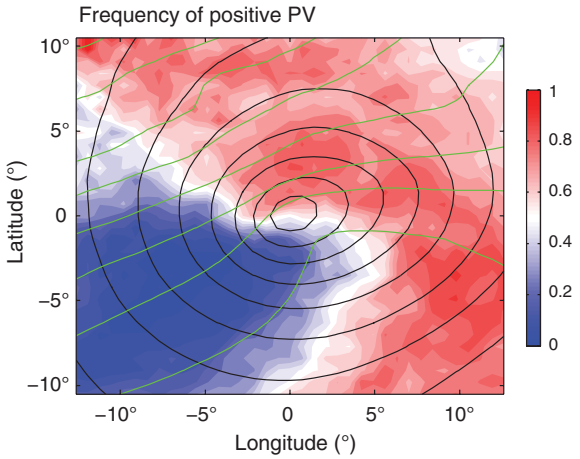

Figure 3. Same as Figure 2(a), with shadings for the frequency of positive PV in the composite.

Bracegirdle (2008), which identifies cold-air outbreaks as the region of lowest low-level static stability, i.e. the highest positive values of $\partial\theta/\partial p$ calculated between the surface and 700 mb.

Figure 5 displays PV in a longitude/height section across the low pressure system (i.e. along the line of zero latitude in Figure 2a). In the warm sector, east of the low pressure (i.e. positive longitude on the x-axis), PV is positive throughout the boundary layer. West

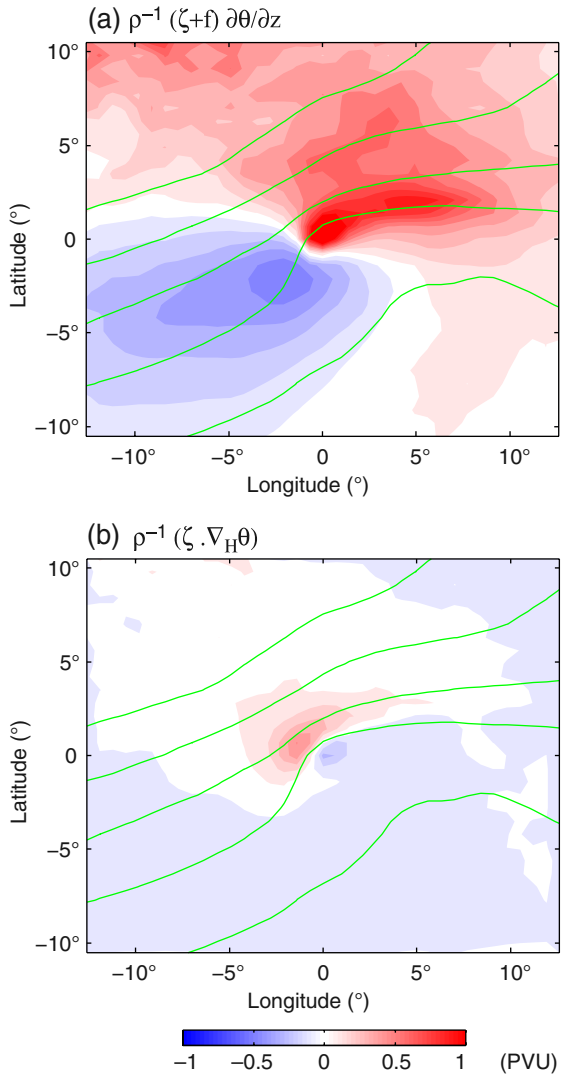

Figure 4. Decomposition of PV at 975 mb for the composite of extratropical storms into the two contributions: (a) PV_Z and (b) PV_H (see text for definitions) and potential temperature (green contours every 5 K).

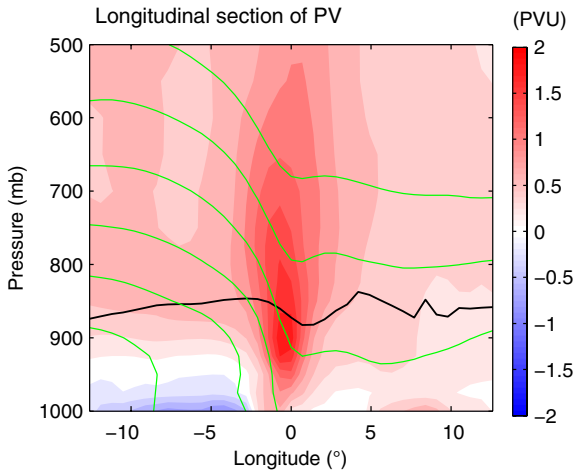

Figure 5. Longitudinal section of the mean potential vorticity (in PVU and represented in shadings) passing through the low-pressure centre of the storm composite (latitude 0° in Figure 2), dry potential temperature (green contours every 5 K) and top of the boundary layer (black line).

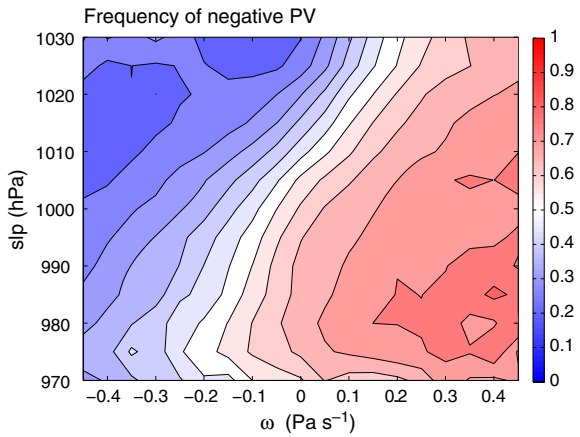

Figure 6. Time frequency of negative PV as a function of local sea-level pressure (in hPa) and mid-tropospheric vertical velocity (ω at 500 mb in Pa s^{-1}). Statistics are calculated over 33 winters and over the Atlantic Ocean in the band of latitude 30–50°.

of the low pressure (negative longitude on the x-axis), there is in contrast a strong vertical gradient of PV in the boundary layer: negative values are found in a shallow layer near the surface and positive values above it. Finally, a column of high PV extends above the low centre up to the mid free troposphere. This feature is reminiscent of the so-called PV tower resulting from the vertical alignment of positive upper-level and low-level PV anomalies (Hoskins *et al.*, 1985; Campa and Wernli, 2012).

We have shown that negative PV was a systematic feature of the cold sector. In order to characterize the cold sector fully, it is also necessary that negative PV be observed primarily there. In order to address this converse relationship, we investigate the sign of PV within particular dynamical regimes. Here, the latter are examined as a function of SLP and vertical velocity in pressure coordinates (ω) at 500 mb. For low SLP values, one expects to find $\omega > 0$ in the cold sector (subsidence) and $\omega < 0$ in the warm sector (WCBs are ascending regions). These expectations are supported by Figure 6, which displays the observed frequency of negative PV for different dynamical regimes (500 mb ω on the x-axis and SLP on the y-axis). One indeed observes that negative PV dominates in regions of subsidence (up to 80% of the time in this regime) and positive PV in regions of ascent (up to 70% of the time). For systems with higher surface pressure (i.e. moving up along the y-axis), positive PV largely dominates and high frequencies of negative PV are confined to strong subsiding regimes.

In the next section, we compute PV tendencies in the boundary layer to explain the origin of the negative PV in the cold sector of storms.

4. PV in the boundary layer

4.1. *PV tendencies*

The usefulness of PV thinking partly relies on its conservation property (Hoskins *et al.*, 1985): PV is conserved for inviscid and adiabatic flows and behaves like a dynamic tracer on isentropes. However, friction and diabatic processes occurring in the atmospheric boundary layer do alter PV, as stated by (Hoskins *et al.*, 1985):

$$\frac{\mathrm{D}PV}{\mathrm{D}t} = \frac{1}{\rho}\left[\boldsymbol{\zeta}_{\mathrm{a}}.\nabla\dot{\theta} + \boldsymbol{F}.\nabla\theta\right], \qquad (2)$$

where $\boldsymbol{\zeta}_{\mathrm{a}}$ and θ were introduced in Eq. (1), $\dot{\theta}$ is the heating rate and $\boldsymbol{F}$ the frictional force.

The main challenge of PV budgets is to separate the different PV sources and sinks and to interpret their impact individually. One possible approach consists of carrying out sensitivity experiments by suppressing a PV source or sink, such as dry atmospheric simulations, to isolate the effect of latent heating (e.g. Kuo *et al.*, 1991; Wernli *et al.*, 2002), or simulations with and without surface turbulent fluxes to isolate the effect of boundary-layer processes (e.g. Plant and Belcher, 2007). Stoelinga (1996) achieved a full partitioning of PV by integrating PV tendencies of the different physical processes in a full physics mescoscale model and inverting them to find the corresponding induced circulation. More recently, a series of articles

(Adamson *et al.*, 2006; Plant and Belcher, 2007; Beare, 2007; Boutle *et al.*, 2007) used the framework of boundary-layer PV tendencies introduced by Cooper *et al.* (1992) to describe boundary-layer PV in dry baroclinic life-cycle models and discuss the relative importance of the different physical processes (turbulent fluxes of heat and momentum). This last approach has the advantage, compared with the first two, that it is applicable to ERA-Interim data offline.

We adapted the Lagrangian PV tendencies in the boundary layer, following the derivation by Cooper *et al.* (1992) and Plant and Belcher (2007) for a dry atmosphere, to include the effect of latent heating. The analytical derivation assumes a uniform density in the boundary layer, ρ_0, as well as a linear decrease of turbulent fluxes of heat and momentum from their surface values. The PV tendency averaged over the boundary layer depth, h, decomposes into

$$\left[\frac{DPV}{Dt}\right] \equiv [G] = \underbrace{-\frac{\Delta\theta\ \hat{\boldsymbol{k}}\,.\,(\boldsymbol{\nabla}\times\boldsymbol{\tau}_S)}{\rho_0^2 h^2}}_{1} \underbrace{-\frac{\boldsymbol{\tau}_S\,.\,(\hat{\boldsymbol{k}}\times\boldsymbol{\nabla}\theta_h)}{\rho_0^2 h^2}}_{2} \underbrace{-\frac{\hat{\boldsymbol{k}}.\,\boldsymbol{\zeta}_a(z=h)H_S}{\rho_0 h^2}}_{3} \underbrace{-\frac{\Delta\boldsymbol{V}\,.\,(\hat{\boldsymbol{k}}\times\boldsymbol{\nabla}H_S)}{\rho_0 h^2}}_{4} + \underbrace{\frac{1}{\rho_0 h}\int_0^h \boldsymbol{\zeta}_a.\,\boldsymbol{\nabla}\dot{\theta}_{lat}\,dz}_{5}, \quad (3)$$

in which the subscript 'S' denotes the values taken at the surface and 'h' at the top of the boundary layer. H_S is the surface sensible heat flux, $\boldsymbol{\tau}_S$ the surface stress vector, $\hat{\boldsymbol{k}}$ the vertical unit vector, $\Delta\boldsymbol{V}$ and $\Delta\theta$ are respectively the difference of horizontal wind and potential temperature between the top of the boundary layer and the Earth's surface and $\dot{\theta}_{lat}$ is the latent heating. The symbol [ ] denotes the vertical average over the depth of the boundary layer.

4.2. *Physical mechanisms*

The physical meaning of the different terms in Eq. (3) was provided by Cooper *et al.* (1992), Adamson *et al.* (2006) and Beare (2007). Here, we give a brief physical interpretation of each tendency term, following the labelling in Eq. (3), and reflect on their relative significance based on the schematic in Figure 7.

(1) In a barotropic vortex, the friction induces Ekman convergence towards the centre of the storm. The first term of Eq. (3) can be thought as the advection of planetary potential vorticity out of the boundary layer by Ekman pumping. Indeed, as shown by Plant and Belcher (2007), the Ekman pumping velocity is defined by

$$w_E = \frac{1}{\rho f}\,\boldsymbol{k}\,.\,(\boldsymbol{\nabla}\times\boldsymbol{\tau}_S),$$

so that the first term can be rewritten as

$$\frac{1}{\rho}(f\Delta\theta w_E).$$

Interpretation is then straightforward after noticing that $(1/\rho)f\Delta\theta$ is the planetary component of the potential vorticity integrated over the depth of the boundary layer.

(2) The second term (often referred to as baroclinic generation of PV by friction) can be interpreted as the Ekman advection of potential temperature. The Ekman transport integrated over the depth of the Ekman layer is given by $u_E = [1/(\rho f)]\,\hat{\boldsymbol{k}}\times\boldsymbol{\tau}_S$. According to Eq. (3), an advection of warm (resp. cold) air in the Ekman layer will reduce (resp. increase) the vertical gradient of potential temperature and give a negative (resp. positive) PV tendency. Figure 7 shows that in the warm sector (northeast) the orientation of Ekman velocity with respect to the strong temperature gradient of the warm front will favour a positive tendency. In the cold sector, where the Ekman velocity is oriented along the isotherms, the contribution of this term to the PV budget is expected to be negligible.

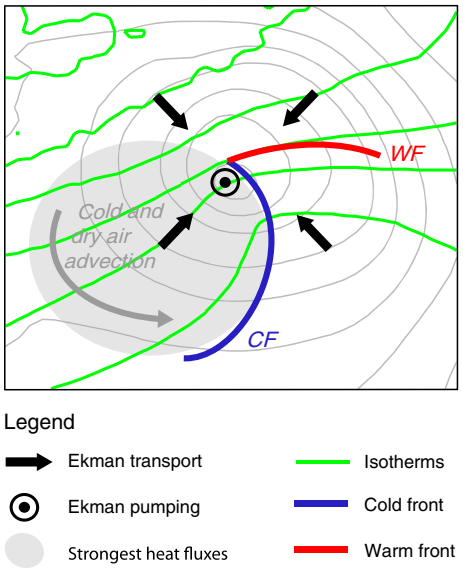

Figure 7. Schematic of the processes leading to PV generation/destruction in the boundary layer of an extratropical storm. See section 4.2 for a description of these processes.

(3) The third term corresponds to the effect of heat fluxes on the thermal stratification. In the cold sector, the strong upward heat fluxes (see Figure 7) will be associated with a negative PV tendency, according to Eq. (3). We expect this destruction of PV to occur via the reduction of static stability in the boundary layer (Plant and Belcher, 2007; Chagnon *et al.*, 2013).

(4) Plant and Belcher (2007) thought of this fourth term as being essentially baroclinic, the main contribution coming from the horizontal variation of the surface layer stability ($T_1 - T_{surface}$). They evaluated its order of magnitude and showed that this term was negligible. This is also what we find in this study.

(5) The fifth term corresponds to the effect of latent heating. Wernli *et al.* (2002) showed that in the storm *Lothar*, which occurred in 1999, continuous and intense condensational heating sustained a pronounced positive low-level PV anomaly, whereas the upper-level cyclone was not modified at an early stage. As the storm strengthened, the upper-level PV anomaly merged with the low-level PV to form a vertically aligned tower of positive PV. Davis *et al.* (1993) showed that the primary effect of condensational heating at low levels was simply to superimpose a positive PV anomaly on the cyclonic circulation that would exist without latent heating. This additional circulation favours interaction between the upper and low-level cyclones, as highlighted in Stoelinga (1996). In the present study, no assumption can be made on the vertical distribution of latent heat release. As latent heating is not provided by ERA-Interim data either, the last term will not be calculated explicitly in this study. If this contribution could be estimated, we would expect the latent heating in the boundary layer to generate positive PV along the WCB and below the level of maximum condensational heating, that is to say along and west of the cold front and above the warm and bent-back front. This would not, therefore, contribute to negative PV tendencies.

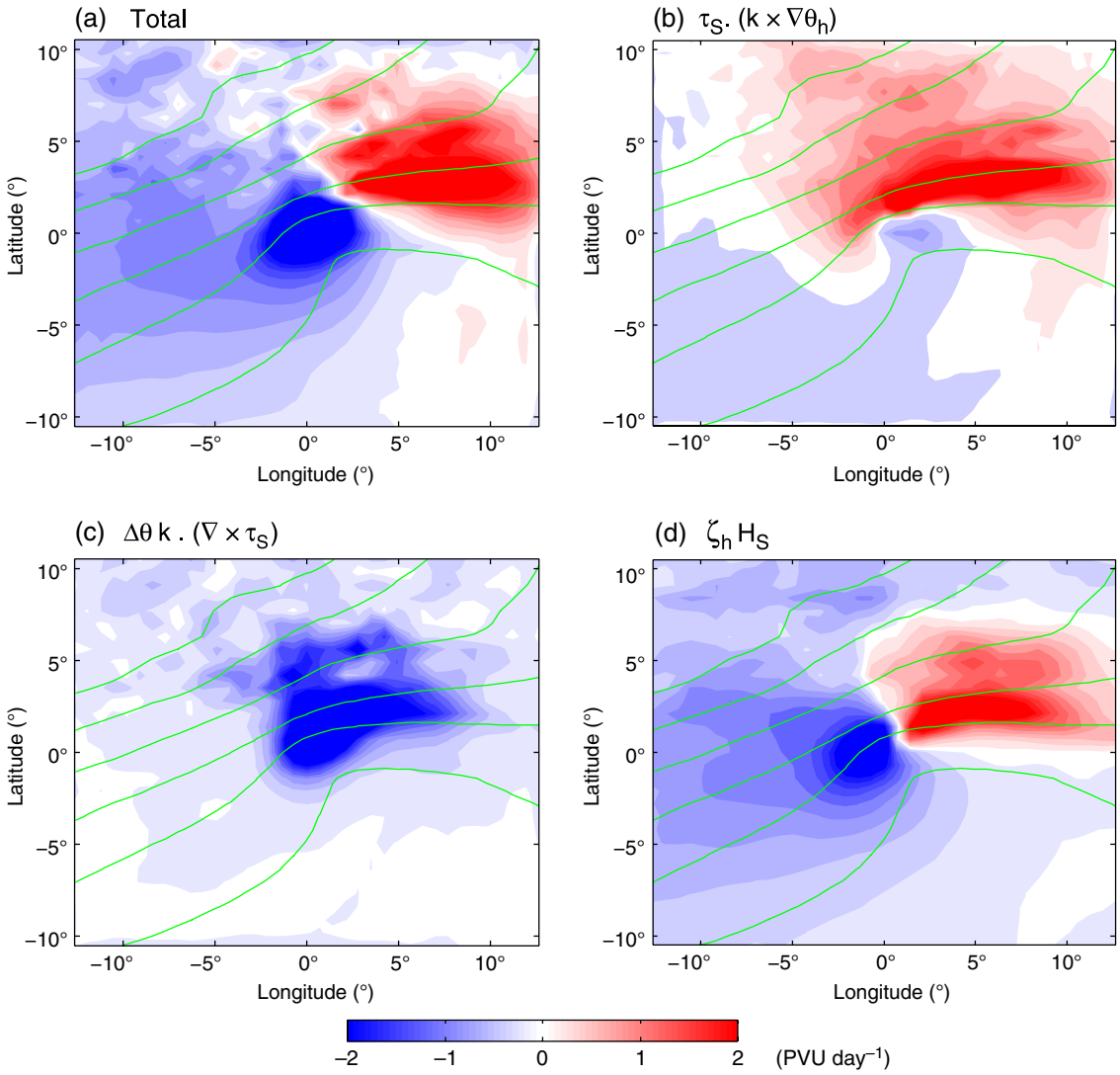

Figure 8. Lagrangian PV tendencies (PVU day^{-1} and represented in shadings) averaged vertically over the boundary-layer depth for the composite of extratropical storms: (a) total PV tendency, (b) baroclinic role of friction, (c) Ekman pumping and (d) barotropic role of heat fluxes, and potential temperature (green contours every 5 K).

4.3. PV tendency integrated in the boundary layer

The total PV tendency integrated in the boundary layer is presented in Figure 8(a). It shows a strong PV reduction at the centre of the storm, surrounded by a dipole PV generation northeast of the low centre and PV destruction southwest of the low centre. This total tendency is further decomposed into the different physical processes presented in the previous section in the remaining panels (b), (c) and (d).

The qualitative role of friction in the intensification or the damping of the storm has been extensively studied by Adamson *et al.* (2006), Beare (2007), Boutle *et al.* (2007) and Plant and Belcher (2007). In these studies, friction is shown to produce positive PV baroclinically on the northeast side of the storm. There, the thermal gradient is strongest and its orientation with regards to the wind stress is favourable for positive PV generation (Adamson *et al.*, 2006; Beare, 2007). ERA-Interim data presented here show similar results to idealized atmospheric simulations (Figure 8(b)).

At the centre of the storm, the PV tendency associated with Ekman pumping leads to PV destruction (Figure 8(c)). This result is consistent with the studies mentioned above, even if it shows only weak positive PV generation east of the storm, unlike what was described in idealized experiments (e.g. Adamson *et al.*, 2006). The positive tendency is actually present in most of the individual cases but disappears by averaging the composite (not shown).

The role of sensible heat fluxes has received less attention. Figure 8(d) shows that their contribution is dominant in the cold sector of the storm, where they drive a negative PV tendency. Heat transferred from the atmosphere to the ocean in the warm sector of the storm generates positive PV.

The order of magnitude of the various PV tendency terms is larger than those found in idealistic studies (up to 5 PVU day^{-1} for the baroclinic friction term, compared with 2 PVU day^{-1} for the mid-growth stage of a LC2 type storm in the study of Plant and Belcher (2007)). One possible explanation is the presence of a strong SST gradient in the region studied here, which enhances the baroclinicity and the intensity of storms. Furthermore, the storms selected in the composite here are among the strongest. The order of magnitude is also larger than estimated by Stoelinga (1996), but we do not expect the magnitude to be exactly the same, as several simplifications have been made in the framework of Cooper's tendencies.

In the PV budget for the boundary layer presented by Plant and Belcher (2007), Cooper's tendency, i.e. the term [G] in Eq. (3), is balanced by the Eulerian PV tendency, the divergence of the horizontal flux of PV and PV transport at the top of the boundary layer. We have computed these three terms (not shown) and found that they exhibit a dipole with positive PV tendency northeast of the low-pressure centre and negative PV tendency southwest and that they have the same order of magnitude as [G]. Both the propagation of the storm, which is mainly northeastward in this region, and its intensification are likely to explain the dipole found in the total PV tendency in Figure 8(a).

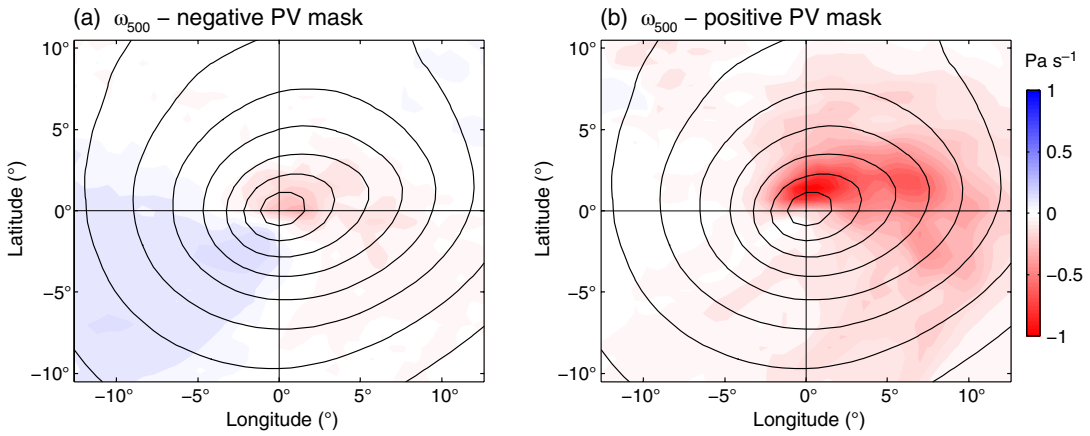

Figure 9. Decomposition of the vertical velocity at 500 mb (in Pa s^{-1}) for the composite of extratropical storms using the PV-based indicator for the cold sector: (a) vertical wind occurring in the cold sector, (b) vertical wind occurring outside the cold sector.

5. Defining an indicator for the cold sector of extratropical storms

5.1. *Application of a PV-based indicator*

As negative PV spans over the cold sector of storms and since it is a systematic and exclusive feature of the cold sector (section 3), it is justified to use it as an indicator of this part of the storm. This indicator will make it possible to partition processes occurring in the cold sector from those occurring in the rest of the storm. For the sake of simplicity and to avoid extrapolating the PV field at the surface, the PV mask is computed with 950 mb PV. Thus, a negative PV mask is created, with the value 1 set where 950 mb PV is negative and 0 where it is positive. Some difficulty may arise from the fact that PV, and hence the position of the cold sector, is calculated every 3 h. As the storm is moving, the cold sector defined instantaneously will not exactly match the variables that are accumulated over intermediate time steps. We will thus first test the application of the PV mask to ω, to ensure the simultaneity of the PV mask and the variable to which it is applied. We will then illustrate another application of the PV mask to variables accumulated over a short period of time (accumulation of large-scale and convective precipitation over the 3 h prior to the time of PV evaluation).

The partitioning of vertical velocity in pressure coordinates (ω) at 500 mb using the PV indicator is shown in Figure 9. The negative PV mask entirely captures the subsidence characterizing the cold sector (Figure 9(a)), whereas the ascending airstream associated with the WCB is well captured by the positive PV mask (Figure 9(b)). However, close to the low centre, ascending motion is also captured by the negative 950 mb PV. This result is not surprising, considering the westward tilt of the system with height: the vertical velocity at 500 mb may be in the cold sector being identified by 950 mb PV. Another possible explanation is that the cyclonically turning branch of the WCB ascends in the free troposphere above the cold sector.

Next, we investigate the use of the PV mask for convective (Figure 10(a)) and large-scale (Figure 10(b)) precipitation, focusing first on the synoptic event described in Figure 1. Where PV is positive, the convective precipitation forms a band easily attributable to the south branch of the WCB and locally reaches 24 mm day^{-1} (Figure 10(a)). Southwest of the low-pressure centre, a patch of convective precipitation reaching 5 mm day^{-1} occurs in the negative PV area. The large-scale precipitation is exclusively located where PV is positive (Figure 10(b)) and exhibits the tau shape characterizing the cyclonically turning branch. Encouraged by these results, we finally estimate the contribution of cold sector processes to climatological convective and large-scale precipitation in Figure 11 by applying the PV mask to the precipitation rates found in the 57 storms discussed in section 3. The distribution of convective precipitation is clearly partitioned in the reference frame of the storm: the southwest quadrant of the storm is seen to experience most of the convective precipitation generated in the cold sector (Figure 11(a)), while the northeastern and southeastern quadrants experience convective precipitation generated outside the cold sector (Figure 11(b)). Despite this physically sound partitioning, the patterns of precipitation revealed by the composites need to be analyzed carefully. Indeed, because the centre of the cyclone is fixed while the relative location of the fronts can vary from one cyclone to another, the shape of the band of precipitation along the cold front is smoothed out. Thus, the maximum of convective precipitation in the composite appears along the warm front, which is relatively stationary with respect to the cyclone centre. Considering the smoothing effect of compositing precipitation, the partitioning of convective precipitation between the cold sector and the rest of the storm is consistent with the snapshot presented in Figure 10: east of the low pressure, convective precipitation corresponds to the south branch of the WCB, while it corresponds to the cold sector southwest of the low pressure.

Large-scale precipitation occurs northeast of the low-pressure centre irrespective of the sign of PV (Figure 11(c) and (d)). This region corresponds to the northern part of the WCB and most of the large-scale precipitation is consistently captured by the positive PV mask. A lesser but not negligible fraction of large-scale precipitation is also captured by the negative PV mask. Analysis of individual events suggests that this precipitation corresponds to the WCB but that it falls in the domain of negative PV (not shown). One possible reason for this erroneous attribution is the westward tilt of the system, as explained above for the vertical velocity. In the next section, we compare the skill of the PV mask at partitioning the vertical motion and the precipitation in storms with that of other possible indicators of the cold sector.

5.2. *Assessment of the PV indicator against other distinctive features of the cold sector*

We have so far used negative PV as an indicator of the cold sector but this is by no means its only signature and other quantities could conceivably perform equally well to indicate the cold sector. These include the following.

(1) **The 2 m temperature anomaly** (hereafter T2M), which is negative in the cold sector due to cold advection. This quantity was used by Vavrus *et al.* (2006) to identify marine cold-air outbreaks. Here the temperature anomaly is computed as the departure from a 33 year climatology.
(2) **Sensible heat flux** (hereafter SHF), which is positive upward in the cold sector due to contrast of the cold air and the warmer waters (Zolina and Gulev, 2003). In contrast, in the warm sector the southerly warm advection tends to be associated with sensible heat flux positive downward.

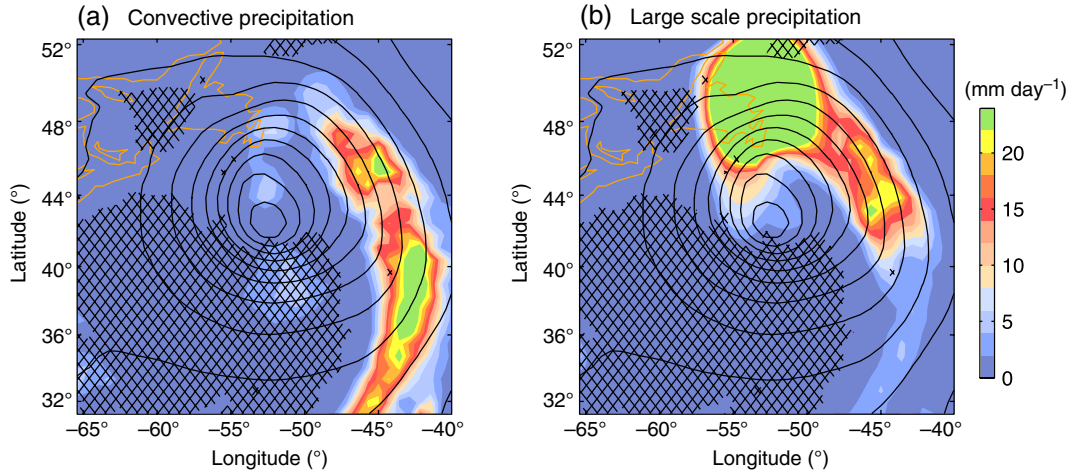

Figure 10. (a) Convective and (b) large-scale precipitation (in mm day^{-1} and represented in shadings), negative PV area used to identify the cold sector (hatchings) and sea-level pressure at 1200 UTC on 20 January 2000 (black contours every 5 mb).

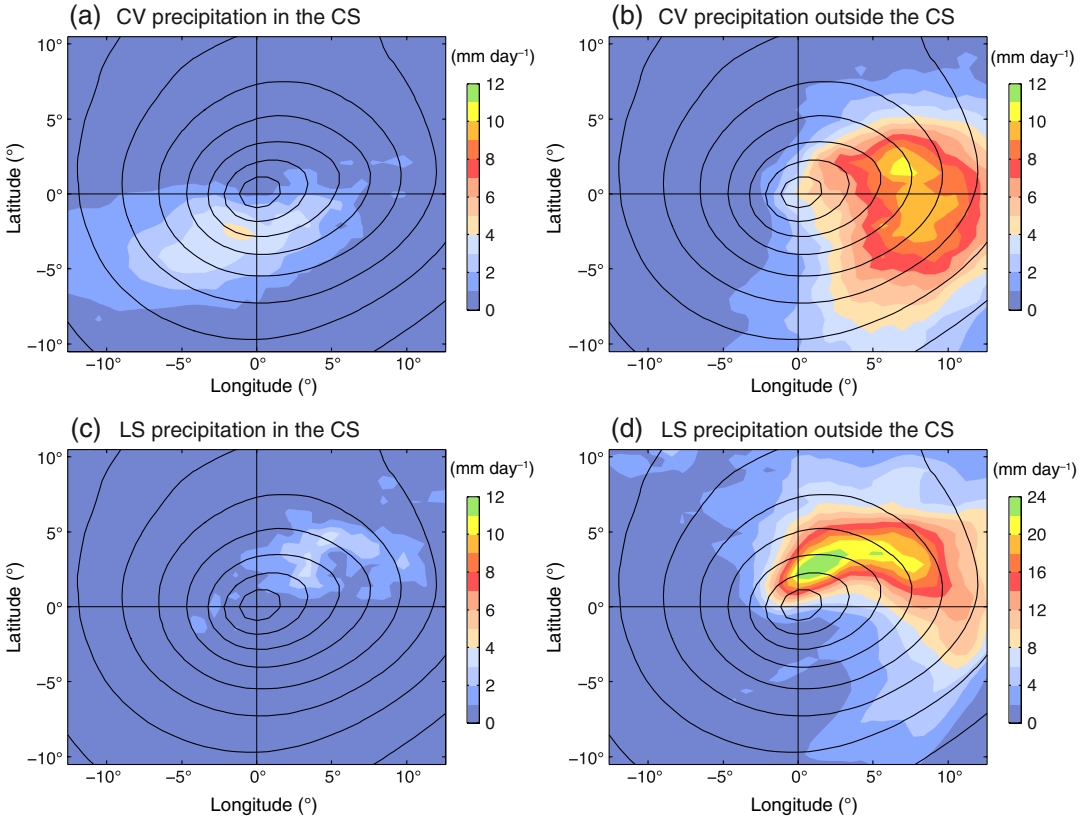

Figure 11. Decomposition of precipitation for the composite of extratropical storms using the PV-based indicator for the cold sector: (a) convective precipitation occurring in the cold sector, (b) convective precipitation outside the cold sector, (c) large-scale precipitation in the cold sector and (d) large-scale precipitation outside the cold sector. Precipitation is in mm day^{-1}. Also shown is sea-level pressure (black contours every 5 mb, same for all panels).

(3) **Low-level static stability** (hereafter STAB), which measures the thermodynamic disequilibrium between the ocean and the atmosphere. Following Bracegirdle and Gray (2008), Kolstad and Bracegirdle (2008) used the difference of potential temperature between the surface and 700 mb. The indicator is computed as follows:

$$\frac{\Delta\theta}{\Delta p} = \frac{\theta_{700} - \theta_{\mathrm{SKT}}}{p_{700} - \mathrm{SLP}},$$

where SLP is the sea-level pressure, p_{700} is 700 mb, θ_{700} is the dry potential temperature at 700 mb and θ_{SKT} is the potential temperature at the surface using skin temperature.

In this section, we achieve a comparison of the performance of all the possible indicators including the PV indicator. Based on the results presented in the previous sections, a good indicator must satisfy the following requirements: detect convective precipitation in the southwest quadrant, minimize large-scale precipitation in the northeast and isolate the mean subsiding motion of the cold sector.

Figure 12 compares the mean convective and large-scale precipitation and vertical wind in the composite of 57 storms. These quantities are averaged in the four quadrants obtained by drawing a vertical and horizontal line that would intersect in the middle of the reference frame of the storm (see Figure 11 for an indication of each quadrant). We find that all these indices are sensitive to the threshold that is applied to single out the cold sector. Despite a somewhat arbitrary choice, we evaluate the different indices with values of the threshold that best fit the three requirements (Figure 12(b)). The values chosen for the threshold of each indicator are given in Table 1.

All diagnostics show that convective precipitation is four times larger than large-scale precipitation in the core of the cold sector

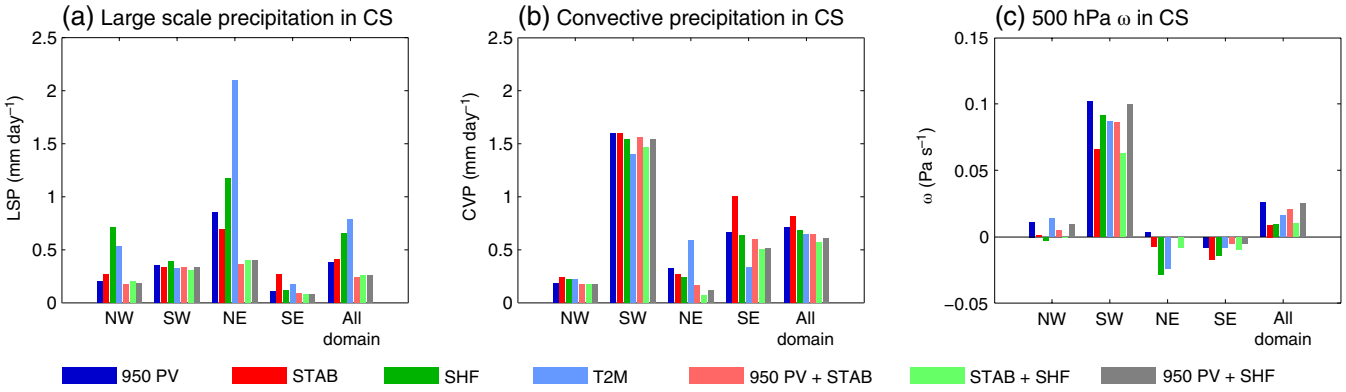

Figure 12. Comparison of the diagnostics of the cold sector: 950 mb PV (PV950), surface sensible heat flux (SHF), 2 m temperature anomaly (T2M) and static stability (STAB). Two extra diagnostics combine the previous diagnostics with different values of the threshold: SHF + STAB combines surface sensible heat flux and static stability diagnostics, whereas PV950 + SHF + STAB combines 950 mb surface sensible heat flux and static stability diagnostics. The different panels show (a) large-scale precipitation (mm day^{-1}), (b) convective precipitation (mm day^{-1}) and (c) vertical wind (Pa s^{-1}). The quantities are averaged in the four quadrants of the reference frame of the storms: northwest, southwest, northeast and southeast, and for the whole reference frame of the storm. See text for more details.

Table 1. Threshold values chosen for the different indicators.

Indicator	Variable	PV (K m^2 s^{-1} kg^{-1})	Sensible heat flux (W m^{-2})	2 m temperature anomaly (K)	Static stability (K mb^{-1})
PV950	PV at 950 mb	<0	–	–	–
SHF	Surface sensible heat flux	–	< −100	–	–
T2M	2 m temperature anomaly	–	–	< −1	–
STAB	Low-level stability	–	–	–	<0.02
SHF + STAB	–	–	< −100	–	<0.02
PV950 + STAB	–	<0	–	–	<0.03
PV950 + SHF	–	<0	< −50	–	–

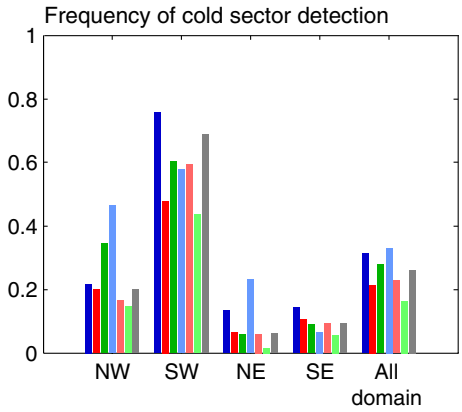

Figure 13. Same as Figure 12, but the frequency of the cold sector being detected by indicators is now plotted.

region (southwestern or SW quadrant) (Figure 12(a) and (b)). All diagnostics also agree that subsidence dominates in the core of the cold sector (SW quadrant).

Inspection of individual events suggests that small differences in convective precipitation and subsidence between the diagnostics occur at the edges of the cold sector (not shown). For large-scale precipitation, some diagnostics (e.g. T2M and SHF) identify precipitation under the cloud head (NE and NW regions, Figure 12(b)) where ω is negative (Figure 12(c)). For convective precipitation, some diagnostics (e.g. STAB) identify convective precipitation under the cold-front cloud band (SE quadrant). The mean ascending wind in the SE quadrant, which is twice as large in STAB as in PV950, is another piece of evidence that STAB erroneously detects the WCB instead of the cold sector.

Ideally, the indicator should be systematic in separating air masses with different features and associated precipitation. The frequency of the detection of the cold sector in the southwest quadrant varies by 25% depending on the indicator considered (Figure 13), PV950 being the most systematic and STAB the least. We point out that for STAB, the frequency of detection of the cold sector in Figure 13 corresponds to the average for each quadrant of the frequency presented in Figure 3, so it is clear that it should not be 100% in the southwest quadrant. Even though PV950 and STAB perform similarly in separating precipitation, the fact that the cold sector is detected less often in STAB impacts the partitioning of other atmospheric variables such as ω (SW region, Figure 12(c)). One may be surprised that PV950 and STAB perform so differently, considering that low-level static stability was shown in section 3 to set the sign of PV at 950 mb. This underscores the role of the horizontal component of PV (PV_H in section 3) in 'spreading' the region of negative PV horizontally (compare Figure 4(b) and Figure 4(a)).

As the indicators exhibit different biases, we explore the possibility of combining two conditions in a single indicator. We discard the 2 m temperature, as the biases associated with this indicator are too large, and we test the three remaining indicators using pairs: STAB + PV950, SHF + PV950 and SHF + STAB. The three coupled indicators give similar results for the mean precipitation in each quadrant (Figure 12(a) and (b)). In addition, they outperform all the single indicators by strongly reducing the amount of large-scale precipitation captured in the entire composite and in the northeast quadrant in particular. This suggests that the biases of indicators taken individually are distributed randomly and largely cancel out when combined. However, a crucial difference between the three combined diagnostics is that the two indicators including PV detect the cold sector more often than the indicator that does not include PV (Figure 13). This has a significant impact on the mean vertical wind captured in the cold sector (compare SW in Figures 12(c) and 13). The more systematic detection of the cold sector by indicators including PV makes us conclude that they are actually the best performing indicators of this region.

In summary, the application of the negative PV mask best matches the theoretical and conceptual expectation that convective precipitation dominates in the cold sector, while large-scale precipitation dominates in the warm sector of extratropical cyclones. The technique is deemed accurate for convective precipitation, but requires more caution for large-scale precipitation. A better partitioning is obtained by combining PV at 950 mb

with another diagnostic of the cold sector, such as the sensible heat flux intensity or a measure of the low-level static stability.

6. Summary and discussion

The presence of negative potential vorticity behind the cold front of extratropical storms, previously reported by a few studies, has been thoroughly documented in ERA-Interim data. Negative PV is a systematic feature of the cold sector and the transition from negative to positive PV across the cold front is sharp. Here, the term 'cold sector' has been used to refer to the portion of the extratropical cyclone behind the cold front. Negative PV is confined to a layer shallower than the boundary layer and the decomposition of the horizontal and vertical dot products of PV, respectively referred to as PV_H and PV_Z in the text, showed that the negative sign of PV in the cold sector is mainly set by the vertical gradient of potential temperature (PV_Z). The horizontal component ($PV_H = \zeta_{\mathrm{H}}.\nabla_H\theta/\rho$) also contributes to the negative PV and it helps to make regions of negative PV more extensive.

The PV tendencies derived by Cooper *et al.* (1992) and computed in ERA-Interim data are consistent with those analyzed in previous idealized numerical experiments: positive PV is generated by baroclinic friction on the northeast side and negative PV is generated at the centre of the storm by Ekman pumping. In addition, we showed that surface sensible heat fluxes generate negative PV in the cold sector of storms by destabilizing the boundary layer.

PV at a low level was tested as a potential indicator of the cold sector of extratropical storms. It gives a good partitioning of subsiding air in the cold sector and ascending air in the WCB. It also highlights the importance of convective precipitation behind the cold front. However, close to the lowest pressure, the ascending WCB passes over the cold sector, so that the negative PV mask also captures ascending air and large-scale precipitation. This is a limitation of the PV indicator to an exact partitioning of precipitation from the cold sector and the WCB.

The PV-based indicator was compared with other distinctive features of the cold sector that could have been used as indicators. Indicators based on 2 m temperature and surface sensible heat flux have a larger bias to detect large scale precipitation in the warm sector than the PV based indicator. Low-level stability provides results comparable to PV in terms of precipitation partitioning, but there is a more systematic detection of the cold sector when the indicator is based on PV. One may wonder why the PV indicator gives such an improvement compared with low-level stability, since fundamentally they both measure the low surface static stability in the cold sector. We suggested that PV_H, although smaller than PV_Z, plays a decisive role in characterizing the cold sector close to the low centre and the cold front, which are the regions where erroneous detection is most frequent.

We further explored the benefit of combining PV at low level with low-level static stability or sensible heat fluxes to improve the identification of the cold sector. The mixed-diagnostic indicators outperform all of the single-diagnostic ones. Even if they result in a similar partitioning of precipitation, the mixed-diagnostic indicators including PV achieve a more systematic detection of the cold sector, which we can take as a measure of success.

One of the limits of all the indicators that we have explored is the somewhat arbitrary definition of the threshold. It is possible that, depending on the basin or the season, different values of the threshold may be more adapted. Moreover, the use of PV itself as a possible indicator for the cold sector may depend on the basin. Indeed, we can speculate that further away from the coast there should be less negative PV in the cold sector of storms: the wintertime air–sea temperature contrast, together with the high SST gradient, favours large heat fluxes in the Western North Atlantic basin and its associated negative PV tendency. Using a negative PV mask to identify the cold sector elsewhere than in the Western North Atlantic basin needs to be analyzed further.

Despite these limitations, it is hoped that the PV-based indicators discussed in this study will help assess the role of cold- and warm-sector physics in setting the climatological features of the North Atlantic storm track.

Acknowledgements

B. Vannière was funded by the National Environment Research Council through the grant NE/J023760/1. We thank three anonymous reviewers for insightful and constructive comments, which have helped us improve our manuscript.

References

Adamson D, Belcher SE, Hoskins BJ, Plant RS. 2006. Boundary-layer friction in midlatitude cyclones. *Q. J. R. Meteorol. Soc.* **132**: 101–124.
Beare RJ. 2007. Boundary layer mechanisms in extratropical cyclones. *Q. J. R. Meteorol. Soc.* **133**: 503–515.
Berrisford P, Dee D, Fielding K, Fuentes M, Kallberg P, Kobayashi S, Uppala S. 2009. The ERA-Interim archive. *ERA Rep. Ser.* **1**: 1–16.
Boutle I, Beare R, Belcher S, Plant R. 2007. A note on boundary-layer friction in baroclinic cyclones. *Q. J. R. Meteorol. Soc.* **133**: 2137–2141.
Bracegirdle TJ, Gray SL. 2008. An objective climatology of the dynamical forcing of polar lows in the Nordic seas. *Int. J. Climatol.* **28**: 1903–1919.
Brayshaw DJ, Hoskins B, Blackburn M. 2011. The basic ingredients of the North Atlantic storm track. Part II: Sea surface temperatures. *J. Atmos. Sci.* **68**: 1784–1805.
Campa J, Wernli H. 2012. A PV perspective on the vertical structure of mature midlatitude cyclones in the Northern Hemisphere. *J. Atmos. Sci.* **69**: 725–740.
Catto JL, Shaffrey LC, Hodges KI. 2010. Can climate models capture the structure of extratropical cyclones?. *J. Clim.* **23**: 1621–1635.
Chagnon J, Gray S, Methven J. 2013. Diabatic processes modifying potential vorticity in a North Atlantic cyclone. *Q. J. R. Meteorol. Soc.* **139**: 1270–1282.
Chelton DB, Schlax MG, Freilich MH, Milliff RF. 2004. Satellite measurements reveal persistent small-scale features in ocean winds. *Science* **303**: 978–983.
Chou BH, Ferguson MP. 1991. Heat fluxes and roll circulations over the western Gulf Stream during an intense cold-air outbreak. *Boundary-Layer Meteorol.* **55**: 255–281.
Cooper IM, Thorpe AJ, Bishop CH. 1992. The role of diffusive effects on potential vorticity in fronts. *Q. J. R. Meteorol. Soc.* **118**: 629–647.
Dacre H, Hawcroft M, Stringer M, Hodges K. 2012. An extratropical cyclone atlas: A tool for illustrating cyclone structure and evolution characteristics. *Bull. Am. Meteorol. Soc.* **93**: 1497–1502.
Davis CA, Stoelinga MT, Kuo YH. 1993. The integrated effect of condensation in numerical simulations of extratropical cyclogenesis. *Mon. Weather Rev.* **121**: 2309–2330.
Eckhardt S, Stohl A, Wernli H, James P, Forster C, Spichtinger N. 2004. A 15-year climatology of warm conveyor belts. *J. Clim.* **17**: 218–237.
Grossman RL, Betts AK. 1990. Air–sea interaction during an extreme cold air outbreak from the eastern coast of the united states. *Mon. Weather Rev.* **118**: 324–342.
Hawcroft M, Shaffrey L, Hodges K, Dacre H. 2012. How much Northern Hemisphere precipitation is associated with extratropical cyclones? *Geophy. Res. Lett.* **39**: L24809, doi: 10.1029/2012GL053866.
Hewson TD. 1998. Objective fronts. *Meteorol. Appl.* **5**: 37–65.
Hoskins BJ, Valdes PJ. 1990. On the existence of storm-tracks. *J. Atmos. Sci.* **47**: 1854–1864.
Hoskins BJ, McIntyre M, Robertson AW. 1985. On the use and significance of isentropic potential vorticity maps. *Q. J. R. Meteorol. Soc.* **111**: 877–946.
Köhler M. 2005. Improved prediction of boundary layer clouds. *ECMWF Newsl.* **104**: 18–22.
Köhler M, Ahlgrimm M, Beljaars A. 2011. Unified treatment of dry convective and stratocumulus-topped boundary layers in the ECMWF model. *Q. J. R. Meteorol. Soc.* **137**: 43–57.
Kolstad EW, Bracegirdle TJ. 2008. Marine cold-air outbreaks in the future: An assessment of IPCC AR4 model results for the Northern Hemisphere. *Clim. Dyn.* **30**: 871–885.
Kuo YH, Shapiro M, Donall EG. 1991. The interaction between baroclinic and diabatic processes in a numerical simulation of a rapidly intensifying extratropical marine cyclone. *Mon. Weather Rev.* **119**: 368–384.
Liu JW, Liu JW, Xie SP, Norris JR, Zhang SP. 2014. Low-level cloud response to the Gulf Stream front in winter using CALIPSO*. *J. Clim.* **27**: 4421–4432.
Madonna E, Wernli H, Joos H, Martius O. 2014. Warm conveyor belts in the ERA-Interim dataset (1979–2010). Part I: Climatology and potential vorticity evolution. *J. Clim.* **27**: 3–26.
Minobe S, Kuwano-Yoshida A, Komori N, Xie SP, Small RJ. 2008. Influence of the Gulf Stream on the troposphere. *Nature* **452**: 206–209.
Minobe S, Miyashita M, Kuwano-Yoshida A, Tokinaga H, Xie SP. 2010. Atmospheric response to the Gulf Stream: Seasonal variations*. *J. Clim.* **23**: 3699–3719.
Nakamura H, Sampe T, Goto A, Ohfuchi W, Xie SP. 2008. On the importance of midlatitude oceanic frontal zones for the mean state and dominant

variability in the tropospheric circulation. *Geophys. Res. Lett.* **35**: L15709, doi: 10.1029/2008GL034010.

Nelson J, He R. 2012. Effect of the Gulf Stream on winter extratropical cyclone outbreaks. *Atmos. Sci. Lett.* **13**: 311–316.

Plant R, Belcher S. 2007. Numerical simulation of baroclinic waves with a parameterized boundary layer. *J. Atmos. Sci.* **64**: 4383–4399.

Simmonds I, Keay K, Tristram Bye JA. 2012. Identification and climatology of Southern Hemisphere mobile fronts in a modern reanalysis. *J. Clim.* **25**: 1945–1962.

Small RJ, deSzoeke SP, Xie SP, O'Neill L, Seo H, Song Q, Cornillon P, Spall M, Minobe S. 2008. Air-sea interaction over ocean fronts and eddies. *Dyn. Atmos. Oceans* **45**: 274–319.

Stoelinga MT. 1996. A potential vorticity-based study of the role of diabatic heating and friction in a numerically simulated baroclinic cyclone. *Mon. Weather Rev.* **124**: 849–874.

Vavrus S, Walsh J, Chapman W, Portis D. 2006. The behavior of extreme cold air outbreaks under greenhouse warming. *Int. J. Climatol.* **26**: 1133–1147.

Wayland RJ, Raman S. 1989. Mean and turbulent structure of a baroclinic marine boundary layer during the 28 January 1986 cold-air outbreak (Gale 86). *Boundary-Layer Meteorol.* **48**: 227–254.

Wernli H, Schwierz C. 2006. Surface cyclones in the ERA-40 dataset (1958–2001). Part I: Novel identification method and global climatology. *J. Atmos. Sci.* **63**: 2486–2507.

Wernli H, Dirren S, Liniger MA, Zillig M. 2002. Dynamical aspects of the life cycle of the winter storm '*Lothar*' (24–26 December 1999). *Q. J. R. Meteorol. Soc.* **128**: 405–429.

Young GS, Sikora TD. 2003. Mesoscale stratocumulus bands caused by Gulf Stream meanders. *Mon. Weather Rev.* **131**: 2177–2191.

Zolina O, Gulev SK. 2003. Synoptic variability of ocean–atmosphere turbulent fluxes associated with atmospheric cyclones. *J. Clim.* **16**: 2717–2734.